Publ. Astron. Soc. Japan (2015) 67 (1), 10 (1–12)
doi: 10.1093/pasj/psu139
Advance Access Publication Date: 2015 January 19

Solar rotation inferred from radial velocities of the Sun-as-a-star during the 2012 May 21 eclipse*

Yoichi Takeda,[1,2,†] Osamu Ohshima,[3] Eiji Kambe,[4] Hiroyuki Toda,[4] Hisashi Koyano,[4] Bun'ei Sato,[5] Yasuhisa Nakamura,[6] Norio Narita,[1,2] and Takashi Sekii[1,2]

[1]National Astronomical Observatory of Japan, 2-21-1 Osawa, Mitaka, Tokyo 181-8588, Japan
[2]The Graduate University for Advanced Studies, 2-21-1 Osawa, Mitaka, Tokyo 181-8588, Japan
[3]Mizushima Technical High School, 1230 Nishi-Achi, Kurashiki, Okayama 710-0807, Japan
[4]Okayama Astrophysical Observatory, National Astronomical Observatory of Japan, Kamogata, Asakuchi, Okayama 719-0232, Japan
[5]Tokyo Institute of Technology, 2-12-1 Ookayama, Meguro-ku, Tokyo 152-8550, Japan
[6]Fukushima University, 1 Kanayagawa, Fukushima, Fukushima 960-1296, Japan

[†]E-mail: takeda.yoichi@nao.ac.jp

Received 2014 July 4; Accepted 2014 October 28

Abstract

With the aim of examining how much information of solar rotation can be obtained purely spectroscopically by observing the Sun-as-a-star during the 2012 May 21 eclipse at Okayama Astrophysical Observatory, we studied the variation of radial velocities (V_r), which were derived by using the iodine-cell technique based on a set of 184 high-dispersion spectra consecutively obtained over a time span of $\sim$4 hr. The resulting $V_r(t)$ was confirmed to show the characteristic variation (Rossiter–McLaughlin effect) caused by time-varying visibility of the solar disk. By comparing the observed $V_r(t)$ curve with the theoretical ones [which were simulated with the latitude (ψ) dependent solar rotation law $\omega_{\rm sidereal}(\psi) = A + B\sin^2\psi$ (degree d^{-1})] we found that the relation $B \simeq -5.5A + 77$ gives the best fit, though separate determinations of A and B were not possible. Since this relationship is consistent with the real values known for the Sun ($A \simeq 14.5$, $B \simeq -2.8$), we may state that our analysis yielded satisfactory results. This consequence may provide the prospect of getting useful information on stellar rotation of eclipsing binaries from radial-velocity studies during eclipse, if many spectra of sufficiently high time-resolution are available.

Key words: eclipses — line: profiles — Sun: rotation — techniques: radial velocities — techniques: spectroscopic

1 Introduction

It is almost 90 years since the peculiar behavior in the radial velocity curve of eclipsing binaries during eclipse was discovered by the pioneering studies of Rossiter (1924) (for β Lyr) and McLaughlin (1924) (for β Per). They called this phenomenon the "rotational effect," since it is caused by the combination of two factors: (a) the visible part of the stellar disk changes during the course of eclipse;

*Based on data collected at Okayama Astrophysical Observatory (NAOJ, Japan).

(b) each point of the disk has its own line-of-sight velocity due to stellar rotation.

More specifically, in a typical eclipsing binary system where the rotation and orbital motion are in the same direction, this effect may be briefly described as follows:[1]

1. At the ingress phase, the radial velocity (starting from net-zero when all of the disk is visible) is generally positive and systematically increases until the maximum value is attained just before the mid-eclipse, since the relative contribution of the receding limb (where the line-of-sight velocity is maximum) becomes more important as the obscured fraction of the remaining part of the disk progressively increases.

2. At the egress phase of eclipse, on the contrary, starting from the most negative value (caused by the approaching limb just re-appeared after mid-eclipse), the net (negative) radial velocity again gradually increases with time as the visible fraction of the remaining part of the disk progressively increases, until it eventually ends with net-zero when the whole disk is visible.

3. At the mid-eclipse near the light minimum between (1) and (2), a conspicuous "leap" is observed, since the radial velocity abruptly changes its sign here from positive to negative.

This effect, which is occasionally called the "Rossiter–McLaughlin (R–M) effect" after the discoverers, recently received the attention of astronomers especially in connection with observations of transiting planets, since it can be applied to diagnose the properties (e.g., rotational velocity, axis of rotation, etc.) of not only the host star but also the planetary system (e.g., Ohta et al. 2005).

Yet, when it comes to eclipsing binaries belonging to the field of stellar physics, studying the properties of the eclipsed component by actively utilizing the R–M effect seems to have been rarely tried so far, despite its conceptual potentiality (e.g., Kallrath & Milone 2009). Is this effect practically applicable to investigating the rotational features (e.g., rotational velocity, degree of differential rotation, etc.) of eclipsing binaries by analyzing the observed radial-velocity curve during the phase of eclipse?

We recently formed the idea of examining this possibility by making use of the unusual occultation phenomenon involving the well-studied and familiar star, the Sun. That is, a deep (but partial) solar eclipse by the Moon took place in the morning of 2012 May 21 and was observed at Okayama Astrophysical Observatory, where sufficient experiences of precise radial velocity determinations by using the 188 cm reflector+ HIDES (HIgh Dispersion Echelle Spectrograph) have been accumulated over more than 10 years thanks to the long-continuing "Okayama Planet Search Program" targeting evolved G–K giants (e.g., Sato et al. 2008). This situation motivated us to carry out a new spectroscopic study on this occasion.

Thus, following our research plan, we first obtained the observed radial velocity curve of the Sun-as-a-star during the course of the eclipse by using HIDES, and then analyzed it to get as much information on the solar rotational properties as possible. The comparison of the results with the actual solar parameters (which we already know very well) makes an interesting and valuable touchstone for discussing the possibility and the prospect of the R–M effect mentioned above. The purpose of this article is to report the consequence of this experiment.

We note that Molaro et al. (2013) recently achieved a successful detection of the R–M effect based on their high-precision radial-velocity observations of integrated sunlight reflected by the Moon during the Venus passage on 2012 June 6. While this study is similar to theirs (though the transiting object is not Venus but the Moon in our case), our aim is different in the sense that it is not only to detect the R–M effect but also to extract therefrom as much information as possible on solar rotation.

2 Observational data

2.1 Observation and spectrum reduction

The detailed data of the partial solar eclipse observed at Okayama Astrophysical Observatory (OAO: longitude = E 133°35′38.″24, latitude = +34°34′34.″12, altitude = 370 m) in the morning of 2012 May 21 (JD 2456068.39–2456068.49 or from ∼6:20 JST to ∼8:50 JST with a duration of ∼2.5 hr) are graphically described in figure 1 (positional changes of the Sun and Moon, variation in the magnitude of eclipse with time, etc.), and the appearances of the Sun at representative phases are schematically depicted in figure 2. All these positional data were generated with the help of HORIZONS operated by NASA/JPL.[2] The aspect angles of the solar rotation axis (P: position angle between the geographic north pole and the solar rotational north pole; B_0: heliographic latitude of the central point of the solar disk) on this day were $P = -19.^{\circ}1$ and $B_0 = -1.^{\circ}95$. On this day, several appreciable active regions (spots, plages, dark filaments, prominences) were observed on the solar surface, as we can see in the Hα filtergram (corresponding to the Hα center) inserted in figure 1, which was taken on 2012 May 21 (at 00:00:36 UT) just after the ending of eclipse by SMART (Solar Magnetic

[1] In this description, we assume that the radial velocity of the whole eclipsing binary system (γ velocity) is zero.

[2] ⟨http://ssd.jpl.nasa.gov/horizons.cgi⟩.

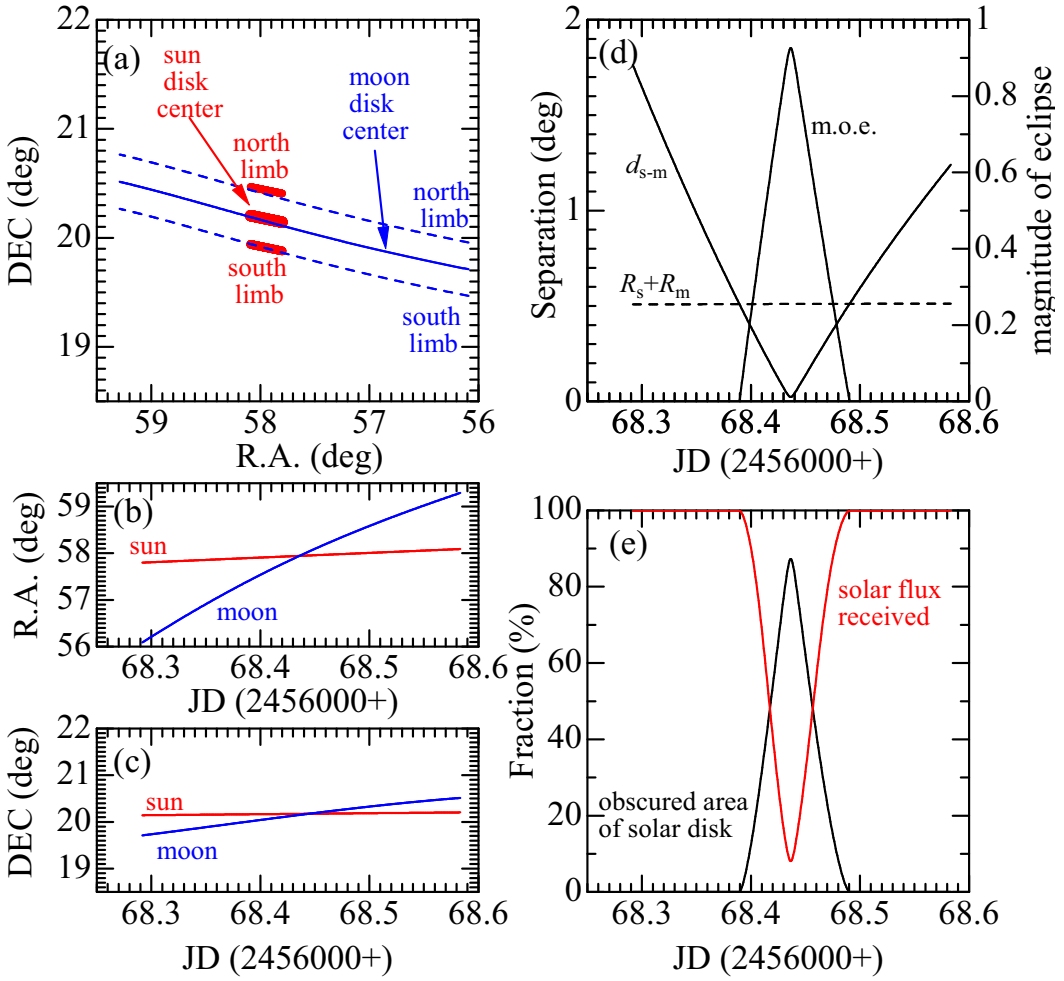

Fig. 1. Graphical description of the solar eclipse at Okayama on 2012 May 21. (a) Tracks of the Sun and Moon on the celestial sphere. (b) Change of right ascension with time. (c) Change of declination with time. (d) Change of Sun–Moon separation ($d_{s\text{-}m}$) and the magnitude of eclipse (m.o.e.), which is defined as $(R_s + R_m - d_{s\text{-}m})/(2R_s)$, with time. (e) Fraction of the Sun's obscured area and that of the total received flux [evaluated by the simple limb-darkening model of equation (8)], plotted against time. (Color online)

Activity Research Telescope) at the Hida Observatory of Kyoto University.[3]

Our spectroscopic observations of the eclipsed Sun were carried out without using the telescope. That is, the bare end of the optical fiber was directly exposed to the solar radiation, so that the collected light was further sent to HIDES via the fiber link system (Kambe et al. 2013). The FOV (field of view) of our observation is a circular area with angular diameter of $\sim 30^\circ$ (corresponding to 0.21 sr; see the explanation below) centered on the Sun. The practical setup of our equipment is described in the following, while graphically depicted in figure 3a (photographic view) and figure 3b (schematic optical layout).

(i) Before the bare input end of the optical fiber [FBP100120140, Polymicro Co. Ltd.; NA (numerical aperture) = 0.22 or f/2.2] toward the Sun, we placed an iodine cell with its vacuum vessel for precise radial velocity measurement.[4]

(ii) As a diffusor, a polishing paper with grain size of 1 μm was inserted between the iodine cell and the fiber. This helped reducing the fiber modal noise considerably as well as decreasing the sunlight by less than one thousandth.

(iii) The FOV of the diffusor was restricted to about ~ 0.21 sr by the vacuum vessel's window, which allowed for monitoring of the whole Sun disk under somewhat poor guidance while considerably limiting the scattered light coming directly from the sky.

(iv) A hole in the filter box (or more exactly, in an aluminum plate just after the vacuum vessel of the iodine

[3] The original image file (filename: "halpha_p00_20120521000036.jpg") is available at ⟨http://www.hida.kyoto-u.ac.jp/SMART/pub/2012/05/21/T1/jpeg/⟩.

[4] This is a copy of the iodine cell described in Kambe et al. (2002).

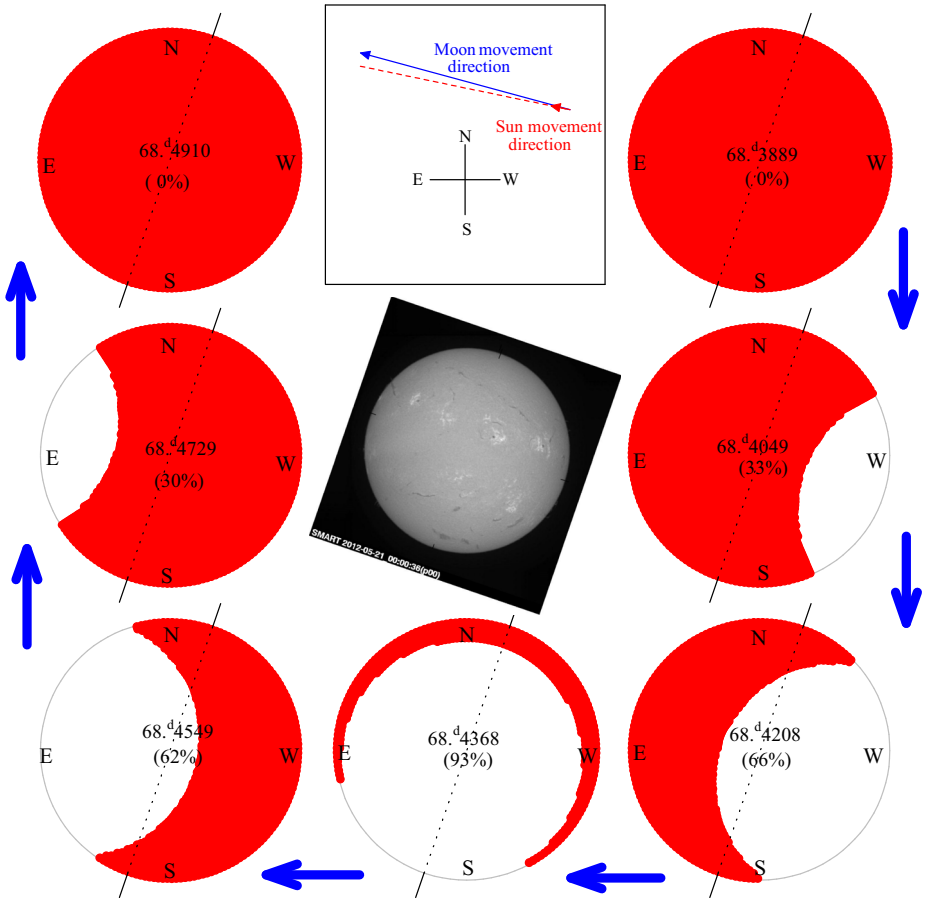

Fig. 2. Schematic display of how the Sun was obscured at seven representative phases of the 2012 May 21 solar eclipse observed at Okayama, where the corresponding Julian day (+2456000) as well as the degree of eclipse are indicated. The direction of the solar rotation axis is also marked on each disk. For a reference, the Hα(-center) filtergram on this day at 00:00:16 UT (just after the ending of eclipse) observed by SMART in Hida observatory of Kyoto University is also presented, in order to indicate the nature of active regions on the solar surface. Shown in the inset are the directions for the movement of the Sun and Moon on the celestial sphere (the latter is by 10.9 times faster than the former). (Color online)

cell) with a diameter of 17 mm, worked as an entrance aperture to the fiber. This assured that the F-ratio of the incident light (f/3.8) was close to that of our normal observations with the telescope and the fiber system.

(v) These fiber-entrance components were put on a portable equatorial telescope mount (Vixen GP.D) for automatically tracking the Sun.

Practically, as we did not have sufficient time to set up the telescope mount properly between the end of the regular night observing run and the solar eclipse, we had to compensate the tracking error manually from time to time. For this purpose, we put pinhole and target plates on the same mount, which were separated by about 200 mm with their axes being aligned to the fiber input end beforehand. We tracked the Sun so that the solar image on the target plate did not move by more than 15′. At the output end of the optical fiber (i.e., at the entrace of the spectrograph), a microlens was used to convert the F-ratio of the incident light to that of the spectrograph (f/29), and then an image slicer was placed to keep a moderate wavelength resolving power. This optics is identical to that of our HIDES fiber-link (Kambe et al. 2013). In this way, we could obtain spectra almost equivalent to those of the Sun seen as a star (solar flux spectra).

Although the observations were done over a time span of $\sim$4 hr (JD 2456068.35–2456068.51 or 5:20–9:20 JST) covering the eclipse, the sky condition was not always suitable, especially before/around the beginning of eclipse where the observations were often disturbed due to clouds. Just after the eclipse began (from $\sim$ JD 2456068.4), however, the condition was significantly improved; from then, we could conduct our observations almost continuously and satisfactorily (even if thin cirrus passed by sometimes). Consequently, we could obtain 184 spectra (with I_2 lines imposed mainly at $\sim$5000–6000 Å) covering 4400–7500 Å with three mosaiced CCDs) with a wavelength resolving power of $R = 52000$. The exposure time for each spectrum frame was set to $\sim$10 s in most cases (while the overhead time for CCD readout was $\sim$40 s).

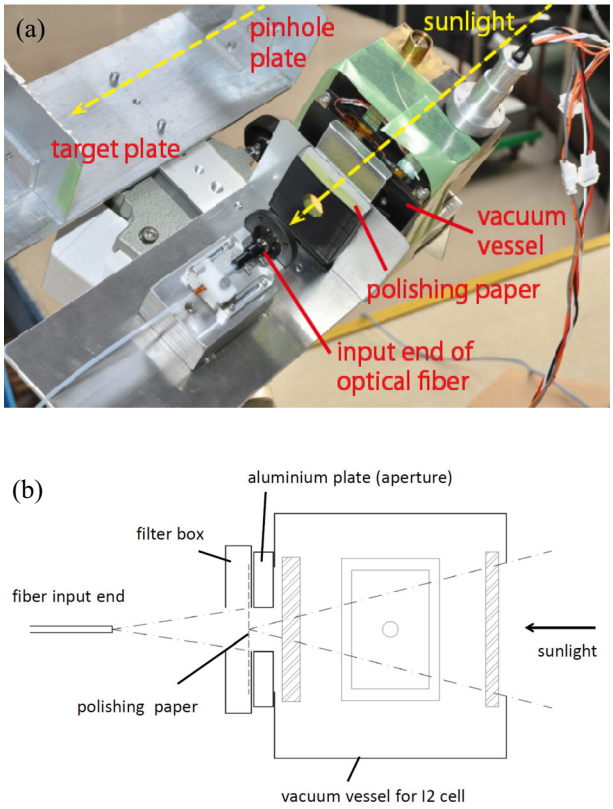

Fig. 3. (a) Photographic view of the fiber entrance components on the portable telescope mount. (b) Schematic optical layout showing how the incident sunlight passes through the I_2 cell and reach the fiber (leading to the spectrograph). See subsection 2.1 for more detailed explanation. (Color online)

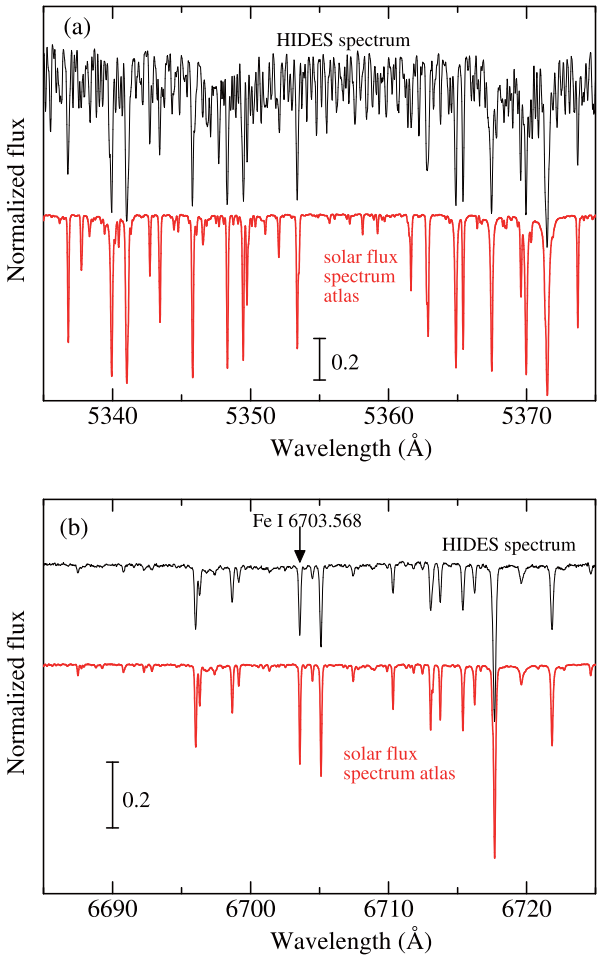

Fig. 4. Typical spectra which we observed with HIDES at JD 2456068.49 (just outside of the eclipse). (a) 5335–5375 Å region (where absorption features of many I_2 molecular lines caused by the iodine cell are manifest). (b) 6685–6725 Å region (where I_2 lines are almost absent). For reference, the solar flux spectra taken from Kurucz et al.'s (1984) atlas are also shown. In panel (b), the position of the Fe I 6703.568 line, for which the line profile was simulated (cf. the Appendix), is also indicated. (Color online)

The reduction of the spectra (bias subtraction, scattered-light correction, aperture determination, flat-field correction, spectrum extraction, wavelength calibration, continuum normalization, etc.) was carried out by using the `echelle` package of IRAF.[5] The typical signal-to-noise ratios (S/N) of the finally resulting spectra are $\sim$400–500 (between minimum $\sim$200 and maximum $\sim$800), as estimated from photon counts at $\lambda \simeq 5500$ Å. As an example, we show in figure 4 one of our typical spectra (taken at just outside of the eclipse) in two wavelength regions of 5335–5375 Å (conspicuous I_2 lines) and 6685–6725 Å (absence of I_2 lines).

As we can see from figure 4, our HIDES spectrum appears similar to Kurucz et al.'s (1984) solar flux spectrum, except that lines in our spectrum are slightly shallower because of the difference in the resolving power. As a more quantitative check, we measured the equivalent widths [EW(OAO)] of $\sim$100 (almost blend-free) Fe I and Fe II lines on our spectrum in $\sim$6200–7400 Å, and compared with those EW(KPNO) measured from Kurucz's (1984) KPNO spectrum atlas, which were already published in Takeda et al. (2005; cf. table E1 therein). We found a fairly good correlation between EW(OAO) and EW(KPNO), as represented by a linear regression relation of $EW(\mathrm{OAO}) = 0.963\ EW(\mathrm{KPNO}) + 1.59$ (where EW is measured in mÅ) with a correlation coefficient of $r = 0.99$. Accordingly, our spectrum may be regarded practically as that of the sunlight integrated over the disk.

2.2 Radial-velocity determination

The radial velocity of the Sun-as-a-star for each frame was derived from the spectrum of $\sim$5000–6000 Å region (where many reference lines of I_2 molecules are manifestly imprinted) basically following the standard procedure (e.g.,

[5] IRAF is distributed by the National Optical Astronomy Observatories, which is operated by the Association of Universities for Research in Astronomy, Inc. under cooperative agreement with the National Science Foundation, USA.

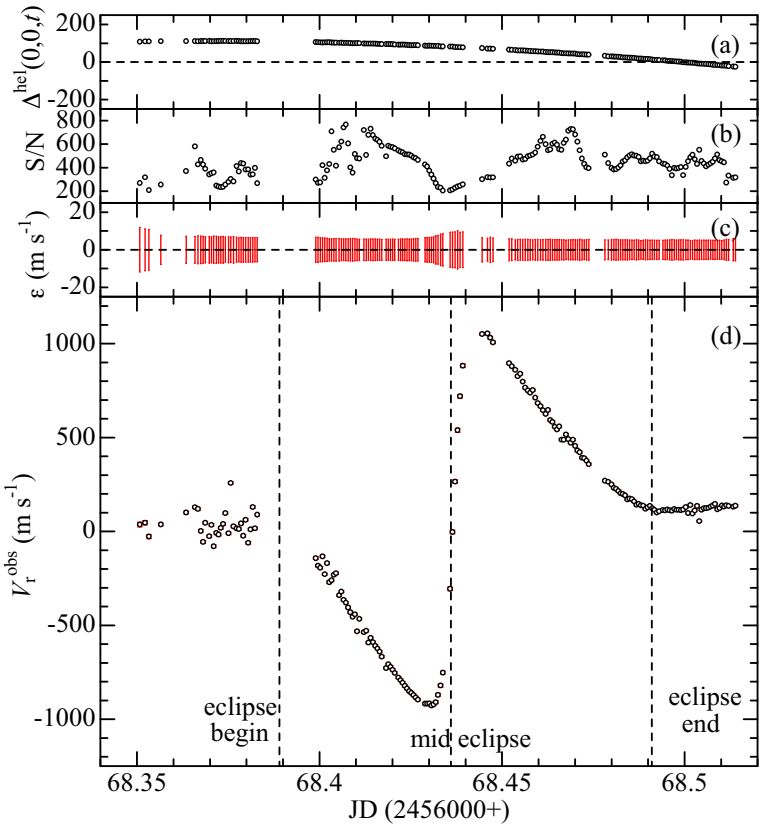

Fig. 5. Run of the observation-related quantities with time. (a) Heliocentric correction due to Earth's motion "at the Sun's disk center" [$\Delta^{hel}(0, 0, t)$; note that this can not be simply applied to V_r^{obs}, as remarked in footnote 9]. (b) S/N ratio of each spectrum estimated from the photon count at $\sim$5500 Å. (c) Estimated error ($\pm\epsilon$) involved with each radial velocity. (d) Observed (uncorrected) radial velocity (V_r^{obs} relative to the template (including an offset constant of -845.5 m s^{-1}), where the error bars [depicted in panel (c)] are attached to the symbols but hardly discernible. Note that the velocity scale in the ordinate of panel (c) is by 10 times expanded as compared to panels (a) and (d). (Color online)

Sato et al. 2002), while using the sky spectrum taken on 2012 January 17 as the template spectrum.[6] The spectrum of the relevant wavelength range was divided into segments of several Ångström, and $\tilde{v}_i$ (radial velocity relative to the template) was determined for each segment i ($i = 1, \ldots, N$). Then, the radial velocity of the Sun-as-a-star relative to that of the template (V_{rel}) and its probable error (ϵ) were computed by averaging these $\tilde{v}_i$ over the segments as follows:

$$V_{rel} \equiv \frac{\sum_{i=1}^{N} \tilde{v}_i}{N} \quad (1)$$

and

$$\epsilon \equiv \sqrt{\frac{\sum_{i=1}^{N} (\tilde{v}_i - V_{rel})^2}{N(N-1)}}. \quad (2)$$

The segments actually used for computing the final result and its error with equations (1) and (2) were carefully chosen by excluding those showing large deviation from the main trend; the number of finally adopted segments was $N = 196$ (about half of the total).

Here, given that only relative time variations are relevant in the present study (cf. footnote 6), we can add any constant to V_{rel} (relative velocity in reference to the template). Actually, these V_{rel} values (i.e., velocity differences between January 17 and May 21) turned out to be rather large, which may be ascribed either to the large time span between observed dates or to some systematic effect because the template spectrum was obtained in the normal mode of HIDES using the 188 cm telescope (i.e., different optical system from that used in this study). Since the time average of V_{rel} over the whole period is $\langle V_{rel} \rangle = 845.5$ km s^{-1}, we apply an offset by this amount and hereafter use $V_r^{obs} (\equiv V_{rel} - 845.5$ km s$^{-1})$ as the formal observed radial velocity, which is convenient because V_r^{obs} outside the eclipse takes values of nearly zero.

The resulting radial velocities V_r^{obs} for all spectra are presented in electronic table (tableE.dat) available online as "Supporting Information," and their variation during the course of eclipse is displayed in figure 5, where the

[6] In radial-velocity determinations based on the I_2-cell technique, only the differential radial velocity of the spectrum is obtained relative to an arbitrarily adopted template spectrum. In this sense, only their time variations are of significance, while the absolute values themselves do not have much meaning.

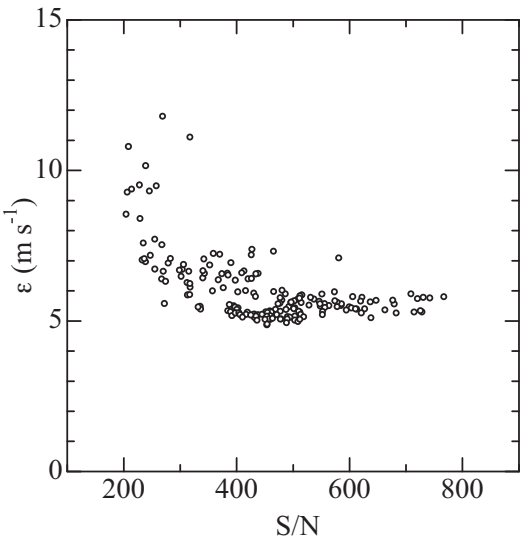

Fig. 6. Correlation between the S/N ratio of each spectrum and the error (ϵ) involved with the derived radial velocity.

related quantities such as S/N and ϵ are also shown. It is evident from figure 5d that the variation of V_r^{obs} has a characteristic shape of the R–M effect (though the sense of change is contrary to what was explained in section 1, since the occultation began from the side of the receding limb in this case).

Regarding the error involved in V_r^{obs}, we can see from figure 5c that ϵ is between ~ 5 m s^{-1} and ~ 10 m s^{-1}, which is about twice as large as that we have normally achieved for similar S/N in our planet search observations. We also note a correlation between ϵ and S/N in the sense that ϵ tends to increase at $S/N \lesssim 300$ (cf. figure 6). Since such cases of comparatively lower S/N correspond to the phases of dimmed sunlight (before the eclipse disturbed by clouds, or near to the mid-eclipse; cf. figure 5), we speculate that differences between the actually observed integrated spectrum and the adopted template sky spectrum may be responsible for this tendency of somewhat larger ϵ (i.e., intrinsic changes of line profiles must have occurred because light contributions from various parts of the disk were inhomogeneously integrated in such cases). At any event, ϵ does not have any significant influence on the essential behavior of V_r^{obs}, as we can see in figure 5d where the error bars are hardly recognized.[7] This observed V_r^{obs} curve will be compared with the simulated theoretical V_r^{cal} in section 4, the computational details for which are described in section 3.

[7] The appreciable fluctuation observed in figure 5d before the beginning of the eclipse (at $\sim$ JD 2456068.37–2456068.38) is not due to errors in V_r^{obs}. This is most probably due to the fact that lights from various parts of the solar disk were inhomogeneously/irregularly contributed in the integrated observed flux, since clumpy clouds were incessantly passing through in front of the Sun at this period.

3 Modeling of radial velocity

We assume that the sidereal angular rotational velocity of the Sun ($\omega_{sidereal}$) depends on the heliographic latitude (ψ) as

$$\omega_{sidereal} = A + B \sin^2 \psi \tag{3}$$

where A and B (in degree d^{-1}) are the parameters corresponding to the equatorial rotation velocity and the degree of differential rotation, respectively.[8]

Since x–y Cartesian coordinate system is defined on the solar disk in such a way that y axis is aligned with the rotational axis (cf. figure 7), the following relation between ψ, x, and y holds (R is the solar radius):

$$R \sin \psi = \sqrt{R^2 - x^2 - y^2} \sin B_0 + y \cos B_0. \tag{4}$$

Then, as the line-of-sight velocity due to solar rotation v_{los} at (x, y) is expressed as

$$v_{los} = x \cos B_0 \, \omega_{sidereal}, \tag{5}$$

we can calculate v_{los} at any point on the solar disk with the help of equations (3), (4), and (5), if A and B are specified.

This $v_{los}(x, y)$ (in the heliocentric system) is then corrected by subtracting the heliocentric correction $\Delta^{hel}(x, y, t)$ due to Earth's motion [not only disk-position-dependent but also time-dependent; computed by following the procedure described in subsection 4.1 of Takeda and Ueno (2011)] to obtain the topocentric value $v_{los}^{topo}(x, y, t)$ corresponding to our observation at Okayama:[9]

$$v_{los}^{topo}(x, y, t) \equiv v_{los}(x, y) - \Delta^{hel}(x, y, t). \tag{6}$$

Consequently, V_r^{cal} (simulated radial velocity of the eclipsed Sun) is evaluated by averaging $v_{los}^{topo}(x, y, t)$ over $D_{vis}(t)$

[8] This two-parameter form is usually adopted to express solar differential rotation determined by the sunspot-tracing method. In case of using the Doppler method where rotation can be investigated up to high-latitude zones, the three-parameter form (with an additional term of $C \sin^4 \psi$) is often applied (e.g., Takeda & Ueno 2011). Here, we decided to adopt the former simpler one.

[9] Namely, $\Delta^{hel}(x, y, t)$ was evaluated by using the "rvcorrect" task of IRAF, while taking into account (i) the rotation of the Earth (diurnal velocity), (ii) the motion of the Earth's center about the Earth–Moon barycenter (lunar velocity), and (iii) the motion of the Earth–Moon barycenter about the center of the Sun (annual velocity). Practically, the heliocentric correction $\Delta^{hel}(x, y, t)$ [for the observation at time t on the disk point (x, y)] was computed at the coordinate $[X_0(t) + x, Y_0(t) + y]$ on the celestial sphere, where $X_0(t)$ and $Y_0(t)$ (the disk-center position of the Sun) were obtained by interpolating the solar ephemeris table. Note that this $\Delta^{hel}(x, y, t)$ can not be simply represented by the disk-center value of $\Delta^{hel}(0, 0, t)$, since it significaltly depends on the position of the solar disk.

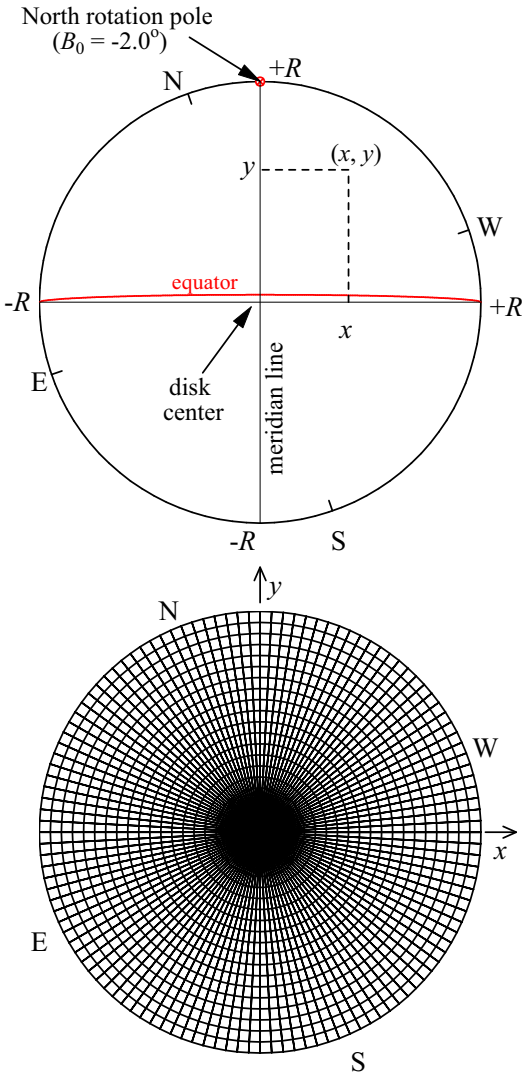

Fig. 7. Coordinate setting and segmentization of the solar disk for simulating the radial velocity (and spectral line profile). Note that the actually adopted division (100 × 360 with steps of 0.01 R and 1°) is by 5 × 3 times finer than that shown here (20 × 120 with steps of 0.05 R and 3°; just to avoid too much complexity). (Color online)

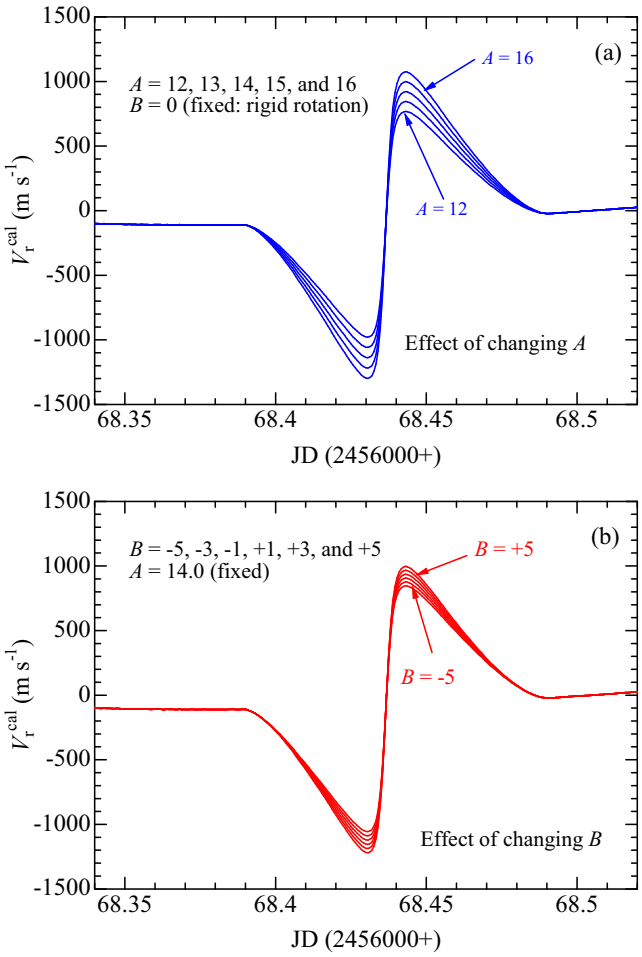

Fig. 8. Run of the theoretically modeled radial velocity with time during the eclipse. (a) Results for five different A values (12, 13, 14, 15, and 16) while B is fixed at 0.0 (rigid rotation). (b) Results for six different B values (−5, −3, −1, +1, +3, and +5) while A is fixed at 14.0. (Color online)

(visible part of the solar disk) while weighting it according to the brightness at each disk point:

$$V_r^{cal}(t) = \frac{\iint_{D_{vis}(t)} v_{los}^{topo}(x, y, t) I(x, y) dxdy}{\iint_{D_{vis}(t)} I(x, y) dxdy}, \quad (7)$$

where the numerical integration was performed by dividing the solar disk into 36000 (≡ 360 × 100 with steps of 1° and 0.01 R) tiny sections (figure 7). Regarding the disk brightness $I(x, y)$, we adopted a linear limb-darkening relation:

$$I(\mu) = I_0(1 - \epsilon + \epsilon\mu), \quad (8)$$

where I_0 is the specific intensity at the disk center, μ is the direction cosine ($\mu \equiv 1 - \sqrt{x^2 + y^2}/R$), and ϵ is the limb-darkening coefficient assumed to be 0.7 (corresponding to $B - V \sim 0.65$ and $\lambda \sim 5000$–6000 Å; cf. figure 17.6 in Gray 2005).[10]

In this way, we could compute V_r^{cal} at any phase of eclipse for various combinations of A and B. Several examples of $V_r^{cal}(t)$ curves are depicted in figure 8a (changing A while B is fixed at 0) and figure 8b (changing B while A is fixed at 14.0).

4 Result and discussion

4.1 Solution search for solar A and B

We are now ready to extract information of (A, B) by comparing V_r^{cal} with V_r^{obs}. For this purpose, we first computed 441 radial velocity curves $V_r^{cal}(t_i)$ ($i = 1, 2, \ldots, N$;

[10] We examined the effect of changing ϵ by ±0.1 on the radial velocity curve, and found that the resulting variation was practically negligible (i.e., ∼6–7 m s^{-1} at most).

$N = 184$ is the number of available spectra for each of the observing times), resulting from combinations of 21 A values (from 12.0 to 16.0 with a step of 0.2) and 21 B values (from -5.0 to $+5.0$ with a step of 0.5). Then, we computed for each case the standard deviation (σ; indicative of the "observation minus calculation residual") defined as

$$\sigma \equiv \sqrt{\frac{\sum_{i=1}^{N}[V_{\rm r}^{\rm obs}(t_i) + C - V_{\rm r}^{\rm cal}(t_i)]^2}{N}}. \tag{9}$$

Here, C is the offset value to be added to $V_{\rm r}^{\rm obs}$ to make the two means ($\langle V_{\rm r}^{\rm obs}\rangle$ and $\langle V_{\rm r}^{\rm cal}\rangle$) equal,[11]

$$C \equiv \frac{\sum_{i=1}^{N}[V_{\rm r}^{\rm cal}(t_i) - V_{\rm r}^{\rm obs}(t_i)]}{N}. \tag{10}$$

Since $\sigma(A, B)$ is a measure of goodness-of-fit between observation and calculation, what we should do next is to find the solutions of (A, B) that minimize σ. After inspection, however, we found it difficult to separately establish the best-fitting values of these two parameters at the same time based on the behavior of σ alone. This situation is illustrated in figure 9, where we can see that the surface of $\sigma(A, B)$ is like an elongated trough, in which pinpointing (A, B) corresponding to σ-minimum is hardly possible. Actually, this is attributed to the fact that both A and B influence the radial velocity curve in a similar manner. That is, as manifested in figure 8, the effect of increasing A (for a fixed B) is qualitatively the same as that of increasing B (for a fixed A), which means that an increase of B can be compensated by an appropriate decrease of A without causing any appreciable change in the shape of $V_{\rm r}^{\rm cal}(t)$. This is the reason for the difficulty of establishing (A, B) from the radial-velocity alone.

Nevertheless, we can at least state that any combination of (A, B) satisfying the equation

$$B \simeq -5.5A + 77 \tag{11}$$

gives the overall best-fit between $V_{\rm r}^{\rm cal}(t)$ and $V_{\rm r}^{\rm obs}(t)$, as shown in the contour diagram of figure 9. Then, how is this relation compared with the real (A, B) values known for the Sun? According to seven representative studies (Ward 1966; Godoli & Mazzucconi 1979; Balthasar & Wöhl 1980; Arévalo et al. 1982; Howard 1984; Balthasar et al. 1986; Sivaraman et al. 1993) where the solar differential rotation was investigated based on the sunspot-tracing method, the resulting (A, B) [in the definition of equation (3)] they determined were in good agreement with each other (cf. figure 12 of Takeda & Ueno 2011), which

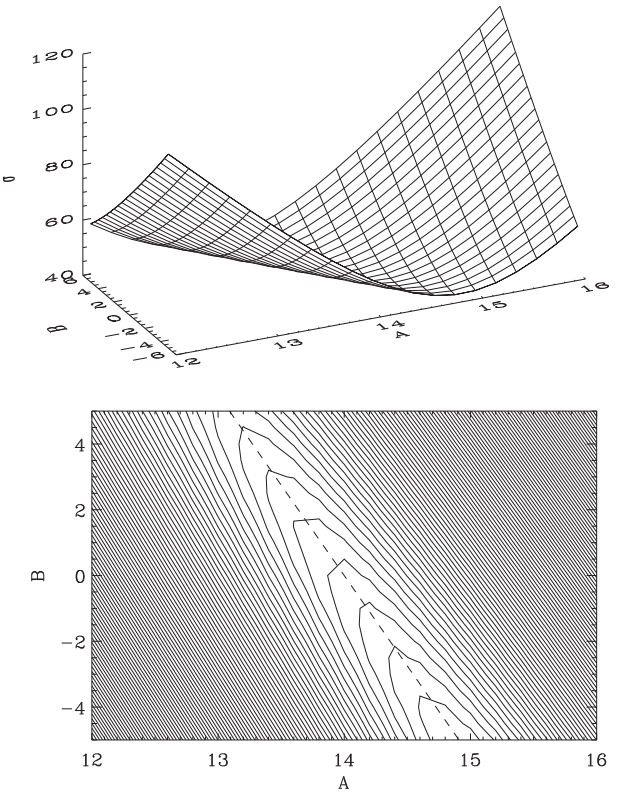

Fig. 9. Graphical representation of the behavior of $\sigma(A, B)$ (standard deviation in fitting the simulated radial velocity curve with the observed data). The upper panel is the 3D representation of the $\sigma(A, B)$ surface, while the lower panel shows the contours of σ on the A–B plane, where the relation $B = -5.5A + 77$ is drawn by dashed line. The unit of σ is m s^{-1}, while that of A and B is degree d^{-1}.

gives $\langle A\rangle = 14.56(\pm 0.04)$ and $\langle B\rangle = -2.81(\pm 0.08)$ on the average (the value with $\pm$ in the parenthesis is the standard deviation). Interestingly, these empirical values are remarkably consistent with equation (11), since it yields $B = -2.75$ for $A = 14.5$. Actually, we can confirm in figure 10 that the $V_{\rm r}^{\rm cal}$ curve computed for $(A, B) = (14.5, -2.75)$ satisfactorily matches our $V_{\rm r}^{\rm obs}$ data.[12]

[11] Note that we can apply any arbitrary constant to $V_{\rm r}^{\rm obs}$, since it is meaningful only in the relative sense.

[12] Precisely speaking, some systematic deviations are noticeable, especially in the first half of observation (before the mid-eclipse); e.g., the observed data are slightly below the theoretical curve at JD 2456068.40–2456068.41, while this tendency is inverted and the amplitude of $V_{\rm r}^{\rm obs}$ is somewhat insufficient at the velocity minimum of JD 2456068.43. Since the fit is more satisfactory for the second half of observation after the mid-eclipse, we suspect that the conditions before and after the mid-eclipse were not strictly symmetrical. It is interesting to note that a similar asymmetric tendency is observed in the comparison of theoretical and observed line-width described in the Appendix. Accordingly, we interpret that this difference of $O - C$ in $V_{\rm r}$ before and after mid-eclipse (worse for the former and better for the latter) was caused because the crescent part being visible just before mid-eclipse happened to include some unusual region (presumably related to active phenomena) which could not be properly treated by our simple modeling. In any event, since the solution is essentially determined by the latter half period after mid-eclipse where the fit is remarkably good, this slight $O - C$ inconsistency just before mid-eclipse does not cause any serious problem.

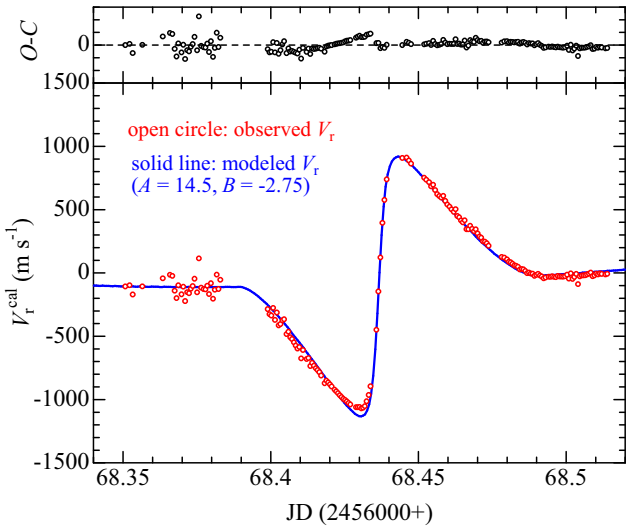

Fig. 10. Demonstration that how the combination of ($A = 14.5$, $B = -2.75$), which is not only consistent with our derived relation [equation (11)] but also the real solution for the actual solar rotation, accomplishes the satisfactory match between the calculation (solid line) and observation (open symbols). In this case, the offset for V_r^{obs} is $C = -143$ m s^{-1} and the standard deviation is $\sigma = 41$ m s^{-1}. (Color online)

4.2 Application of R–M effect to eclipsing binaries

As we have shown above, we could successfully derive the realistic relation between A and B (describing the nature of solar rotation) based on the radial velocity data of the Sun-as-a-star (showing the typical R–M effect) alone, which were obtained during the 2012 May 21 solar eclipse, though separate determinations of A and B were not possible. Then, how is the prospect of applying the R–M effect for studying the rotational properties of eclipsing binaries?

First, we would point out that useful information on the equatorial rotation velocity (v_{eq}) can be obtained by using the R–M effect even if the nature of differential rotation is unknown, since the latter effect on the radial velocity curve is quantitatively less significant (e.g., compare figure 8b with figure 8a). Let us suppose in the present case that B is unknown and we had to assume the rigid rotation ($B = 0$). Then, we would obtain $A = 14.0$ from equation (11), which differs from the true A value only by $\sim 4\%$. Alternatively, it may be reasonable to assume $-B/A \simeq 0.2$ (solar case) for analyzing the R–M effect of general eclipsing binaries, which would not cause any serious error, since the differential rotation parameter of A–F stars studied by Ammler-von Eiff and Reiners (2012) (which they call α, being equivalent to $-B/A$) ranges from ~ 0.0 to ~ 0.5. Considering that spectroscopic determination of $v_{eq} \sin i$ (though i is often known and near $\sim 90^\circ$ for eclipsing binaries) with a precision of $\lesssim 10\%$ based on spectral line profiles is very difficult (especially for double-line binaries where spectral lines of both components are blended and spectra are appreciably time-variable), v_{eq} determination by utilizing the R–M effect would be valuable from the viewpoint of its accuracy.

On the other hand, we expect it to be much more difficult to get information on the differential rotation based on the R–M effect alone. Of course, determination of B might be possible if A (or equatorial rotation velocity) is precisely known in advance based on some other independent way, which, however, does not seem easy in general cases. Rather, we consider that this R–M effect may be useful to "check" the detailed rotational features established by other more sophisticated methods such as magnetic Doppler imaging (making use of the spectrum variation caused by stellar rotation and starspots) based on high-dispersion spectro-polarimetry (e.g., Donati & Collier Cameron 1997; Collier Cameron & Donati 2002).

Here, we should recall that many eclipsing binaries (especially binaries of shorter periods) are tidally locked, so that the rotation and orbital motion are synchronized. If this is already known firmly, it may not be meaningful to determine the rotational velocity or the differential parameter in an independent way. Yet, the accomplishment of co-rotation is not necessarily evident in general cases, especially for the case of young binaries, for which direct confirmation of the rotational parameters based on the R–M effect should still be meaningful. For example, in the case where the tidal synchronization is realized, we should obtain $v_{eq} (\propto A) = 2\pi R/P_{orbital}$ and $B = 0$. It would thus provide the most definite evidence for the existence of co-rotation to confirm these two conditions.

Finally, it should be kept in mind that an R–M effect analysis such as done in this study presupposes an availability of observational data satisfying rather high requirements (a series of many high dispersion spectra with sufficiently high S/N ratios, which have to be obtained in sufficiently high time resolution), since the time-variable radial velocity at each eclipse phase should be determined precisely. Considering that many interesting eclipsing binaries are comparatively faint (and that the integrated star light appreciably gets dimmer during the eclipse), these demands may appear somewhat too severe. Yet, such observations would become practically feasible when observing times of large 8–10 m class telescopes equipped with high-speed spectrometers are flexibly available.

Acknowledgments

We express our heartfelt thanks to Dr. Akihiko Fukui for his help in preparing the observation. EK is grateful for financial support by the Grant-in-Aid for Scientific Research (No. 20540240) from the Japan Society for the Promotion of Science (JSPS). NN

acknowledges support by NAOJ Fellowship, Inoue Science Research Award, and Grant-in-Aid for Scientific Research (A) (No. 25247026) from the Ministry of Education, Culture, Sports, Science and Technology (MEXT).

Appendix. Behavior of spectral line width during eclipse

As a supplementary analysis to our radial velocity study, we also examined (based on our observational data) how the width of a spectral line varies during the eclipse and whether it can be reproduced by theoretical simulations. Since we want to measure the line width influenced by the Doppler motion due to solar rotation, the spectral line should neither be too strong (to avoid large intrinsic width such as the case of a saturated line) nor too weak (to allow a sufficiently precise measurement). Considering these requirements, we selected the Fe I line at 6703.568 Å ($\chi_{\rm low} = 2.76$ eV) for this purpose, which is in the wavelength region almost unaffected by I_2 lines (cf. figure 4b).

We computed the intrinsic line profile (of specific intensity) at each point of the solar disk (where the same division was used as in figure 7) by using Kurucz's (1993) ATLAS9 solar model [$T_{\rm eff} = 5780$ K (effective temperature), $\log g = 4.44$ (logarithmic surface gravity in cm s^{-2}), $v_{\rm t} = 1$ km s^{-1} (microturbulence), [Fe/H] = 0 (metallicity)], which was further convolved with the radial-tangential mactoturbulence function (parameterized with $\zeta_{\rm R}$ and $\zeta_{\rm T}$; cf. Gray 2005) as well as the Gaussian instrumental profile corresponding to $R = 52000$, and finally integrated over the visible disk to get the final profile. In this computation, we adopted an adjusted (astrophysical) $\log gf$ value of -2.90; that is, Kurucz and Bell's (1995) original $\log gf$ of -3.16 was increased by $+0.26$ dex, so that the observed line strength can be reproduced for the solar Fe abundance of $\log \epsilon = 7.50$. Regarding the macroturbulence parameters, we assumed $\zeta_{\rm R} = 2$ km s^{-1} and $\zeta_{\rm T} = 3$ km s^{-1} by consulting figure 2 of Takeda (1995), while considering that the mean-forming depth of this line is $\log \tau_{5000} \sim -1$. As to the combination of (A, B), three representative cases satisfying equation (11) were simulated: (13.0, +5.5), (14.0, 0.0), and (15.0, −5.5).

We then calculated the FWHMs for each of the resulting theoretical profiles corresponding to various eclipse phases, which are to be compared with the observed FWHMs directly measured from our 184 spectra. Such comparisons are displayed in figure 11a, where we can see that the line width shows a variation with the following characteristics:

(i) At the ingress phase, it first decreases gradually until attaining a minimum width around ∼JD 245668.42 where only the approaching east limb is visible (near to the minimum $V_{\rm r}$).

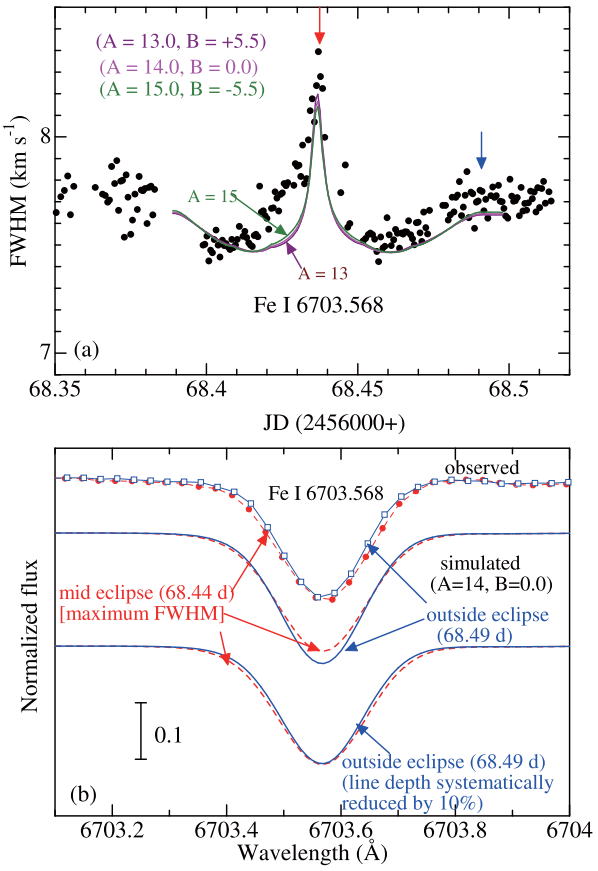

Fig. 11. (a) Comparison of the observed (symbols) and simulated (lines) FWHM of Fe I 6703.568 during the course of eclipse. The modeled curves are computed with three different (A, B) combinations of (13.0, +5.5), (14.0, 0.0), and (15.0, −5.5) satisfying equation (11). (b) Comparison of the Fe I 6703.568 line profiles at two representative phases indicated by downward arrows in panel (a) (mid-eclipse with the largest FWHM at JD 2456068.44 and outside of eclipse at JD 2456068.49). Top: observed profiles (line-connected filled and open symbols correspond to mid- and outside-eclipse, respectively). Middle: theoretical profiles (the dashed and solid lines correspond to mid- and outside-eclipse, respectively). Bottom: almost the same as the middle, but the line depth of the stronger one (solid line) is intentionally reduced by 10% in order to make the direct comparison of both FWHM easier. (Color online)

(ii) Then it turns to grow as the receding west limb begins to reappear, and eventually shows a maximum sharp peak at the mid-eclipse (at JD 245668.44) where both the approaching east limb and the receding west limb are equally visible.

(iii) After that, in the egress phase, the width decreases abruptly and again becomes minimum around ∼JD 245668.46 when only the receding west limb is visible (near to the maximum $V_{\rm r}$), then begins to gradually increase toward the eclipse end.

It is immediately noticed from figure 11a that the mutual differences between the FWHM curves computed for three (A, B) combinations are very subtle and hardly discernible. Thus the situation is quite the same as that of the case of

the radial velocity, meaning that separate determinations of (A, B) based on the FWHM analysis are not possible.

According to the comparison shown in this figure, our observed FWHM data surely exhibit such an expected qualitative tendency, though not necessarily satisfactory in the quantitative sense. Especially, the deviation is appreciable at the phases before the mid eclipse (JD 2456068.42–2456068.43), while a more or less tolerable consistency is observed after the mid-eclipse. It is interesting that this asymmetric situation is somewhat similar to the case of figure 10 as mentioned in subsection 4.2 (footnote 12). We also point out that the line depth is expected to become slightly larger at the mid-eclipse compared to the value outside of the eclipse according to our calculation, which is not observed in our spectra (cf. figure 11b). This may imply that our line-profile modeling needs to be further improved if much better fitting is to be pursued.

Supporting Information

Additional Supporting Information may be found in the online version of this article:

tableE.dat and **readme_tableE-txt**.

Please note: Oxford University Press are not responsible for the content or functionality of any supporting materials supplied by the authors. Any queries (other than missing material) should be directed to the corresponding author for the article.

References

Ammler-von Eiff, M., & Reiners, A. 2012, A&A, 542, A116

Arévalo, M. J., Gomez, R., Vázquez, M., Balthasar, H., & Wöhl, H. 1982, A&A, 111, 266

Balthasar, H., Vázquez, M., & Wöhl, H. 1986, A&A, 155, 87

Balthasar, H., & Wöhl, H. 1980, A&A, 92, 111

Collier Cameron, A., & Donati, J.-F. 2002, MNRAS, 329, 23

Donati, J.-F., & Collier Cameron, A. 1997, MNRAS, 291, 1

Godoli, G., & Mazzucconi, F. 1979, Sol. Phys., 64, 247

Gray, D. F. 2005, The Observation and Analysis of Stellar Photospheres, 3rd ed. (Cambridge: Cambridge University Press)

Howard, R. 1984, ARA&A, 22, 131

Kallrath, J., & Milone, E. F. 2009, Eclipsing Binary Stars: Modeling and Analysis, 2nd ed. (New York: Springer)

Kambe, E., et al. 2002, PASJ, 54, 865

Kambe, E., et al. 2013, PASJ, 65, 15

Kurucz, R. L. 1993, Kurucz CD-ROM, No. 13 (Cambridge: Harvard-Smithsonian Center for Astrophysics)

Kurucz, R. L., & Bell, B. 1995, Kurucz CD-ROM, No. 23 (Cambridge: Harvard-Smithsonian Center for Astrophysics)

Kurucz, R. L., Furenlid, I., Brault, J., & Testerman, L. 1984, Solar Flux Atlas from 296 to 1300 nm, (Sunspot, NM: National Solar Observatory)

McLaughlin, D. B. 1924, ApJ, 60, 22

Molaro, P., Monaco, L., Barbieri, M., & Zaggia, S. 2013, MNRAS, 429, L79

Ohta, Y., Taruya, A., & Suto, Y. 2005, ApJ, 622, 1118

Rossiter, R. A. 1924, ApJ, 60, 15

Sato, B., et al. 2008, in Extreme Solar Systems, ASP Conf. Ser., 398, ed. D. Fischer et al. (San Francisco: ASP), 67

Sato, B., Kambe, E., Takeda, Y., Izumiura, H., & Ando, H. 2002, PASJ, 54, 873

Sivaraman, K. R., Gupta, S. S., & Howard, R. F. 1993, Sol. Phys., 146, 27

Takeda, Y. 1995, PASJ, 47, 337

Takeda, Y., Ohkubo, M., Sato, B., Kambe, E., & Sadakane, K. 2005, PASJ, 57, 27

Takeda, Y., & Ueno, S. 2011, Sol. Phys., 270, 447

Ward, F. 1966, ApJ, 145, 416